Chapter 6

MHD Darcy-Forchheimer hybrid nanoliquid flow over an elongated permeable sheet in a porous medium with hydrodynamic slip constraint *

6.1 Introduction

Modified Buongiorno nanoliquid model (MBNM) extends the traditional Buongiorno model by considering the effectual slip mechanisms along with the effective properties of a nanofluid. The dynamics of hydromagnetic Darcy-Forchheimer hybrid nanoliquid flow over an elongated permeable sheet with hydrodynamic slip constraint has been studied. The passive control of nanoparticle volume fraction at the boundary yields a realistic and practical model. In addition, the introduction of the modified Buongiorno model makes the present work different from the existing literature. The statistical scrutinization on the surface drag involving injection/suction effects, with the aid of regression analysis, enhances the novelty and uniqueness of the current exploration. The current study finds its applications in astronomical disciplines, fuel injection, thermal protection, and aerodynamics . A comparative analysis of the velocity profile on the two-dimensional and axisymmetric flows in the presence of slip and no-slip constraints has also been presented. The main objectives of the current study are to:

*Published in: Waves in Random and Complex Media (Taylor & Francis), 2022; (early access)

- Construct a mathematical model to study the dynamics of hydromagnetic Darcy-Forchheimer hybrid nanoliquid flow over an elongated permeable sheet in the presence of hydrodynamic slip using MBNM and passive control of nanoparticles.
- Conduct a comparative analysis on the nanoliquid flow by examining the injection and suction effect.
- Explore the influence of pertinent parameters on flow profiles.
- Utilize regression analysis to obtain a correlation between the influential parameters and the drag coefficient.

6.2 Mathematical formulation

A three-dimensional steady laminar incompressible and electrically conducting viscous nanofluid flow past a lengthening sheet in a Dacry-Forchheimer porous medium is analyzed. Let (u, v, w) be the velocity components along (x, y, z) directions. The sheet is stretched with velocities $U_w = ax$ and $V_w = by$ along x- and y- directions, respectively. Partial velocity slip with slip coefficient N_1 is considered at the boundary. A permeable sheet with mass flux velocity $w_0 > 0$ (for injection) and $w_0 < 0$ (for suction) is considered. A magnetic field of uniform strength B_0 is considered along the z-direction. The induced magnetic field was neglected due to the small magnetic Reynolds number. The hybrid nanoliquid flow is modeled using MBNM and a physically more realistic boundary condition that passively controls the volume fraction of nanoparticles. The convective boundary constraint that creates a significant relation between thermal difference and heat flux at the surface (see (Zhao et al., 2022)) is also incorporated. The temperature at the sheet is regulated with a convective heating condition by utilizing hot fluid. The physical configuration of the model is illustrated in Fig 6.1.

The boundary layer equations describing the fluid flow are as follows (see (Kumar et al., 2021), (Jusoh, Nazar, & Pop, 2018), (P. Rana, Mahanthesh, Mackolil, & Al-Kouz, 2021), (Muhammad, Alsaedi, Hayat, & Shehzad, 2017)):

$$u_x + v_y + w_z = 0 \tag{6.2.1}$$

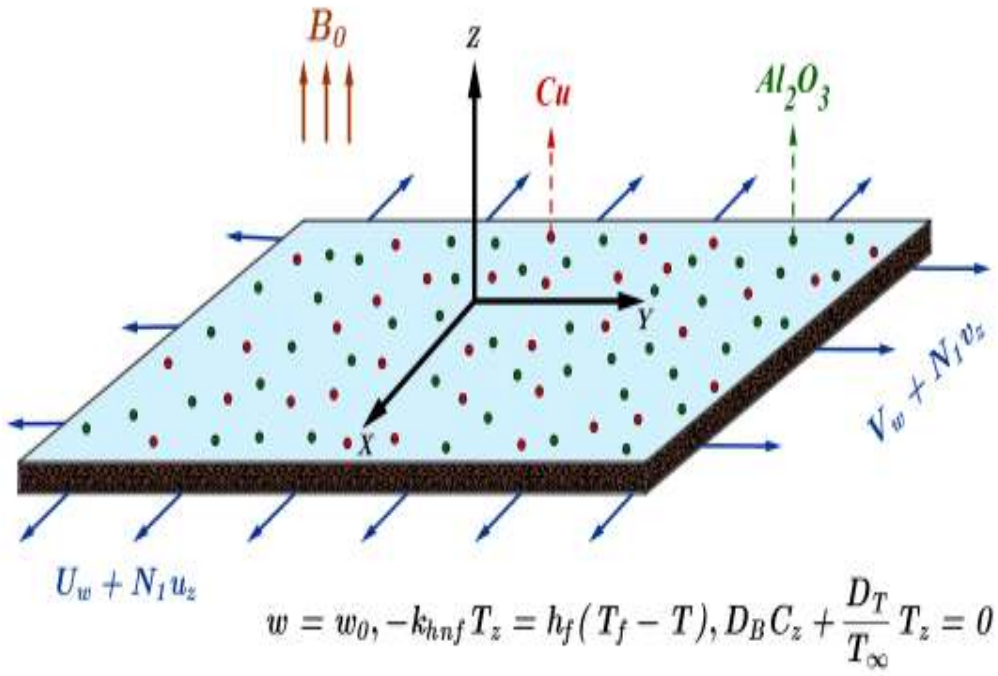

Figure 6.1: *Physical configuration.*

$$\rho_{hnf}\left(uu_x + vu_y + wu_z\right) = \mu_{hnf}\left(u_{zz} - \frac{u}{K_p}\right) - \sigma_{hnf}B_0^2 u - \frac{\rho_{hnf}\, C_b^* u^2}{x\sqrt{K_p}} \tag{6.2.2}$$

$$\rho_{hnf}\left(uv_x + vv_y + wv_z\right) = \mu_{hnf}\left(v_{zz} - \frac{v}{K_p}\right) - \sigma_{hnf}B_0^2 v - \frac{\rho_{hnf}\, C_b^* v^2}{y\sqrt{K_p}} \tag{6.2.3}$$

$$uT_x + vT_y + wT_z = \frac{k_{hnf}}{(\rho C_p)_{hnf}}T_{zz} + \frac{(\rho C_p)_p}{(\rho C_p)_{hnf}}\left\{\frac{D_T}{T_\infty}T_z^2 + D_B T_z \mathcal{C}_Z\right\} \tag{6.2.4}$$

$$u\mathcal{C}_x + v\mathcal{C}_y + w\mathcal{C}_z = D_B\mathcal{C}_{zz} + \frac{D_T}{T_\infty}T_{zz} \tag{6.2.5}$$

with the corresponding boundary conditions:

$$\left.\begin{array}{l} u = ax + N_1 u_z \ ,\ v = by + N_1 v_z \ ,\ w = w_0 \ , \\ -k_{hnf}T_z = h_f\left(T_f - T\right) \ ,\ \frac{D_T}{T_\infty}T_z + D_B\mathcal{C}_z = 0 \ . \end{array}\right\} \ at\ z = 0 \tag{6.2.6}$$

$$u \to 0 \ ,\ v \to 0 \ ,\ T \to T_\infty \ ,\ \mathcal{C} \to \mathcal{C}_\infty \ . \qquad as\ z \to \infty. \tag{6.2.7}$$

The quantities of physical interest are the skin friction coefficients (Cf_x and Cf_y) and the Nusselt number (Nu_x) quantifying the surface drag and rate of heat transfer at the sheet, respectively are given by (see (Jusoh et al., 2018), (Yusuf, Mabood, Khan, & Gbadeyan, 2020)):

$$Cf_x = \frac{\tau_{wx}}{\rho_f U_w^2} = \frac{\mu_{hnf}\left(\frac{\partial u}{\partial z}\right)_{z=0}}{\rho_f U_w^2} \ , \tag{6.2.8}$$

$$Cf_y = \frac{\tau_{wy}}{\rho_f V_w^2} = \frac{\mu_{hnf}\left(\frac{\partial v}{\partial z}\right)_{z=0}}{\rho_f V_w^2} \ , \tag{6.2.9}$$

$$Nu_x = \frac{x q_w}{k_f\left(T_f - T_\infty\right)} = \frac{-x\ k_{hnf}\left(\frac{\partial T}{\partial z}\right)_{z=0}}{k_f\left(T_f - T_\infty\right)} \ . \tag{6.2.10}$$

where τ_{wx} , τ_{wy} , and q_w are the shear stress along the x- and y- directions and the heat flux from the surface, respectively.

The effective thermophysical properties of the hybrid nanoliquid (with alumina as nanoparticle 1 and copper as nanoparticle 2) are given by table 6.1 (see (Mathew et al., 2021), (Aladdin et al., 2020)):

Now consider the following similarity variables (see (Muhammad et al., 2017)):

$$\left.\begin{array}{c} u = axf'\left(\zeta\ \right)\ ,\ v = ayg'\left(\zeta\ \right)\ ,\ w = -\sqrt{a\nu_f}\left(f\left(\zeta\ \right) + g\left(\zeta\right)\right)\ , \\ \zeta = \sqrt{\frac{a}{\nu_f}}\ z\ ,\ \theta\left(\zeta\right) = \frac{T-T_\infty}{T_f - T_\infty}\ ,\ \phi\left(\zeta\right) = \frac{\mathcal{C}-\mathcal{C}_\infty}{\mathcal{C}_\infty}\ . \end{array}\right\} \tag{6.2.11}$$

In view of equation (6.2.11) and the thermophysical properties, one can get the following from equations (6.2.1)-(6.2.10):

$$f''' - \left(\frac{A_2}{A_1}\right)\left\{\left(1 + Fr\right) f'^2 - \left(f + g\right) f''\right\} - \left(\frac{A_3}{A_1} M + K_1\right) f' = 0 \tag{6.2.12}$$

$$g''' - \left(\frac{A_2}{A_1}\right)\left\{\left(1 + Fr\right) g'^2 - \left(f + g\right) g''\right\} - \left(\frac{A_3}{A_1} M + K_1\right) g' = 0 \tag{6.2.13}$$

$$\theta'' + \frac{Pr}{A_4}\left\{A_5\ \left(f + g\right)\theta' + Nt\ \theta'^2 + Nb\ \theta'\phi'\right\} = 0 \tag{6.2.14}$$

$$\phi'' + \left\{Sc\left(f + g\right)\phi' + \frac{Nt}{Nb}\theta''\right\} = 0 \tag{6.2.15}$$

Table 6.1: *The effective thermophysical properties of the hybrid nanoliquid (with alumina as nanoparticle 1 and copper as nanoparticle 2)*

Effective Dynamic Viscosity	$\frac{\mu_{hnf}}{\mu_f} = \frac{1}{\left(1-\phi_{Al_2O_3}\right)^{2.5}(1-\phi_{Cu})^{2.5}} = A_1.$
Effective Density	$\frac{\rho_{hnf}}{\rho_f} = (1-\phi_{Cu})\left((1-\phi_{Al_2O_3}) + \phi_{Al_2O_3}\,\frac{\rho_{s_1}}{\rho_f}\right) + \phi_{Cu}\frac{\rho_{s_2}}{\rho_f} = A_2$
Effective Electrical Conductivity	$\frac{\sigma_{hnf}}{\sigma_f} = 1 + \frac{3\left(\frac{\phi_{Al_2O_3}\sigma_{s_1}+\phi_{Cu}\sigma_{s_2}}{\sigma_f} - \left(\phi_{Al_3O_3}+\phi_{Cu}\right)\right)}{2+\left(\frac{\phi_{Al_2O_3}\sigma_{s_1}+\phi_{Cu}\sigma_{s_2}}{\left(\phi_{Al_2O_3}+\phi_{Cu}\right)\sigma_f}\right) - \left(\frac{\phi_{Al_2O_3}\sigma_{s_1}+\phi_{Cu}\sigma_{s_2}}{\sigma_f} - \left(\phi_{Al_2O_3}+\phi_{Cu}\right)\right)} = A_3$
Effective Thermal Conductivity	$\frac{k_{hnf}}{k_f} = A_4$, where $\frac{k_{hnf}}{k_{nf}} = \frac{k_{s_2}+2k_{nf}-2\phi_{Cu}\left(k_{nf}-k_{s_2}\right)}{k_{s_2}+2k_{nf}+\phi_{Cu}\left(k_{nf}-k_{s_2}\right)}$ and $\frac{k_{nf}}{k_f} = \frac{k_{s_1}+2k_f-2\phi_{Al_2O_3}\left(k_f-k_{s_1}\right)}{k_{s_1}+2k_f+\phi_{Al_2O_3}\left(k_f-k_{s_1}\right)}$
Effective Specific Heat	$\frac{(\rho C_p)_{hnf}}{(\rho C_p)_f} = (1-\phi_{Cu})\left(1-\phi_{Al_2O_3}+\phi_{Al_2O_3}\frac{(\rho C_p)_{s1}}{(\rho C_p)_f}\right) + \phi_{Cu}\frac{(\rho C_p)_{s_2}}{(\rho C_p)_f} = A_5\ .$

with

$$\left.\begin{array}{c} f(0)+g(0)=\lambda\ ,\quad f^{'}(0)=1+b_1 f''(0)\ ,\ g'(0)=\delta+b_1 g''(0)\ , \\ A_4\theta'(0)=Bi\left(\theta(0)-1\right)\ ,\ \phi'(0)+\frac{Nt}{Nb}\theta'(0)=0. \end{array}\right\} \tag{6.2.16}$$

$$f'(\infty\ )\to 0\ ,\ g'(\infty)\to 0\ ,\ \theta(\infty)\to 0\ ,\ \phi(\infty)\to 0 \tag{6.2.17}$$

The subsequent physical quantities are yielded as:

$$Re_x^{\frac{1}{2}}\ \ Cf_x = A_1 f''(0)\ \ ;where\ \ Re_x = \frac{U_w\ x}{\nu_f}\ .. \tag{6.2.18}$$

$$Re_y^{\frac{1}{2}}\ Cf_y = A_1(\delta)^{-\frac{3}{2}} g''(0)\ \ ;where\ \ Re_y = \frac{V_w\ y}{\nu_f}\ . \tag{6.2.19}$$

$$Re_x^{-\ \frac{1}{2}}\ Nu_x = -A_4\theta'(0)\ \ ;\ where\ \ Re_x = \frac{U_w\ x}{\nu_f}\ . \tag{6.2.20}$$

where M (Hartmann number)$= \frac{\sigma_f B_0^2}{a\rho_f}$, K_1 (porosity parameter)$= \frac{\nu_f}{aK_p}$, Nb (Brownian motion parameter)$= \frac{\tau D_B \mathcal{C}_\infty}{\nu_f}$, Pr (Prandtl number)$= \frac{(\mu C)_f}{k_f}$, Fr (Forchheimer parameter)=

$\frac{C_b^*}{\sqrt{K_p}}$, Sc (Schmidt number)= $\frac{\nu_f}{D_B}$, Nt (thermophoresis parameter)= $\frac{\tau D_T\left(T_f - T_\infty\right)}{T_\infty \nu_f}$, τ (effective heat capacity ratio) = $\frac{(\rho C_p)_p}{(\rho C_p)_f}$,b_1 (hydrodynamic slip parameter)= $N_1\sqrt{\frac{a}{\nu_f}}$,

δ (stretching ratio parameter)= $\frac{b}{a}$, Bi (Biot number)= $\frac{h}{k_f}\sqrt{\frac{\nu_f}{a}}$, and λ (suction/injection parameter)= $-\frac{w_0}{\sqrt{a\nu_f}}$ are the non-dimensional parameters.

Table 6.2: *Thermophysical properties of water, alumina, and copper (Aziz et al., 2021), (Aaiza et al., 2015), (Hussanan et al., 2017)*

Property	Base fluid(H_2O)	Nanoparticle 1 (Al_2O_3)	Nanoparticle 2(Cu)
ρ	997.1	3970	8933
C_p	4179	765	385
k	0.613	40	401
σ	0.05	3.5×10^7	5.96×10^7 .

6.3 Numerical solution

The highly nonlinear ODEs given in Eqns. (6.2.12)-(6.2.17) are reduced to a system of single-order ODEs by setting:

$f = y_1, f' = y_2, f'' = y_3,\ g = y_4, g' = y_5,\ g'' = y_6,$

$\theta = y_7,\ \theta' = y_8,\ \psi = y_9, \psi' = y_{10}$ The subsequent system of first-order ODEs is given by:

$$\left.\begin{array}{c} y_1' = y_2\ ,\ y_2' = y_3\ ,\ y_3' = \left(\frac{A_2}{A_1}\right)\left\{(1+Fr)\,y_2^2 - (y_1+y_4)\,y_3\right\} + \left(\frac{A_3}{A_1}M + K_1\right)y_2\ , \\ y_4' = y_5\ ,\ y_5' = y_6\ ,\ y_6' = \left(\frac{A_2}{A_1}\right)\left\{(1+Fr)\,y_5^2 - (y_1+y_4)\,y_6\right\} + \left(\frac{A_3}{A_1}M + K_1\right)y_5\ , \\ y_7' = y_8\ ,\ y_8' = -\frac{Pr}{A_4}\left\{A_5\ (y_1+y_4)\,y_8 + Nty_8^2 + Nb\ y_8 y_{10}\right\}\ ,\ y_9' = y_{10}\ , \\ y_{10}' = -\left\{Sc\,(y_1+y_4)\,y_{10} - \left(\frac{Nt}{Nb}\frac{Pr}{A_4}\right)\left\{A_5\ (y_1+y_4)\,y_8 + Nty_8^2 + Nb\ y_8 y_{10}\right\}\right\} \end{array}\right\} \tag{6.3.1}$$

with

$$\left.\begin{array}{c} y_1(0) + y_4(0) = \lambda\ ,\ y_2(0) = 1 + b_1\ y_3(0)\ \ ,\ y_5(0) = \delta + b_1\ y_6(0)\ , \\ A_4\ y_8(0) = Bi\,(y_7(0) - 1)\ \ ,\ y_{10}(0) + \frac{Nt}{Nb}\ y_8(0) = 0\ . \end{array}\right\} \tag{6.3.2}$$

$$y_2(\infty) \to 0\ ,\ y_5(\infty) \to 0\ ,\ y_7(\infty) \to 0\ ,\ y_9(\infty) \to 0 \tag{6.3.3}$$

The reduced system of first-order ODES is resolved using the bvp5c routine with an error tolerance of 10^{-6}. The bvp5c routine (an efficient built-in MATLAB code

Table 6.3: *Resemblance of* $-Re_x^{\frac{1}{2}}\ Cf_x$ *and* $-Re_y^{\frac{1}{2}}\ Cf_y$ *for differing values of* K_1 , Fr , *and* δ *when* $M = Nt = \lambda = \phi_{Al_2O_3} = \phi_{Cu} = b_1 = Bi = 0$, $Pr = Sc = 1$, *and* $Nb \to 0$.

K_1	Fr	δ	Present study		(Muhammad et al., 2017)	
			$-Re_x^{\frac{1}{2}}Cf_x$	$-Re_y^{\frac{1}{2}}Cf_y$	$-Re_x^{\frac{1}{2}}Cf_x$	$-Re_y^{\frac{1}{2}}Cf_y$
0	0.1	0.2	1.06954	1.67611	1.06945	1.67684
0.1	0.1	0.2	1.11475	1.81692	1.11471	1.81669
0.2	0.1	0.2	1.15832	1.94732	1.15830	1.94722
0.2	0	0.2	1.13043	1.93424	1.13041	1.93414
0.2	0.1	0.2	1.15832	1.94732	1.15830	1.94722
0.2	0.2	0.2	1.18563	1.96045	1.18561	1.96037
0.2	0.1	0.1	1.14163	2.5425	1.14160	2.54234
0.2	0.1	0.3	1.17451	1.7024	1.17449	1.70234
0.2	0.1	0.5	1.20565	1.47624	1.20563	1.47621

Table 6.4: *Resemblance of* $Re_x^{-\frac{1}{2}}\ Nu_x$ *for differing values of* K_1 , Fr , *and* δ *when* $M = \lambda = \phi_{Al_2O_3} = \phi_{Cu} = b_1 = 0$, $Pr = Sc = 1$, $Bi = 0.3$, $Nt = 0.2$, *and* $Nb = 0.5$.

K_1	Fr	δ	$Re_x^{-\frac{1}{2}}\ Nu_x$	
			Present study	(Muhammad et al., 2017)
0	0.1	0.2	0.2045108	0.20448
0.2	0.1	0.2	0.2025510	0.20248
0.2	0	0.2	0.2028408	0.20278
0.2	0.2	0.2	0.2022676	0.20220
0.2	0.1	0	0.1947498	0.19458
0.2	0.1	0.3	0.2056478	0.20560

used for numerical computation) is a finite-difference based code that implements the Lobatto IIIa formula of sixth-order in four steps. ζ_∞ has been restricted to 7 to get an asymptotic solution. The accuracy of the adopted numerical method has been validated through a restrictive correspondence with the previously published results by (Muhammad et al., 2017) and a commendable agreement is observed (see Tables 6.3 and 6.4).

6.4 Results and discussion

The consequence of pertinent parameters on physical quantities, x-directional velocity ($f'(\zeta)$), y-directional velocity ($g'(\zeta)$), temperature ($\theta(\zeta)$), and concentration ($\phi(\zeta)$) profiles are illustrated with the aid of graphs (see Figs. 6.2-6.18) and tables (see Tables 6.5 and 6.6). The Prandtl number (Pr) and Schmidt number (Sc) are set at

6.2 and 2.4, respectively. The thermophysical properties of base fluid (water), Al_2O_3 (nanoparticle 1), and Cu (nanoparticle 2) are given in Table 6.2. The results are presented to compare the flow phenomenon for injection ($\lambda < 0$) and suction ($\lambda > 0$) cases. It is observed that the suction case exhibits lower temperature and velocity profiles which are in perfect harmony with the findings of (Hussanan, Salleh, Khan, & Shafie, 2018). By increasing λ values, the boundary layer thickness diminishes thereby lowering the velocity. Furthermore, a progressive thinning of the thermal boundary layer is noted with an increase in λ values due to the introduction of cold ambient fluid near the sheet.

An increase in ϕ_{Cu} escalates the viscosity of fluid that demotes the velocity profile (see Fig. 6.2). Fig. 6.3 depicts the negative impact of M on $f'(\zeta)$, meaning an increase in M descends the x-directional velocity. This decrease in velocity is due to the generation of Lorentz force. The decreasing nature of $f'(\zeta)$ with Fr has been elucidated in Fig. 6.4. Augmentation in Fr ascends the resistance experienced in the fluid motion and hence $f'(\zeta)$ reduces. Fig. 6.5 describes the decreasing nature of K_1 on $f'(\zeta)$. Fig. 6.6 bespeaks the deviations in $f'(\zeta)$ with respect to b_1. It can be perceived that $f'(\zeta)$ decreases as b_1 values increase. Physically, the hydrodynamic slip parameter reduces the fluid movement due to the roughness of the sheet.

The generation of Lorentz force due to augmenting values of M reduces the y-directional velocity (see Fig. 6.7). The influence of K_1 on $g'(\zeta)$ is analyzed by means of Fig. 6.8. K_1 tends to decrease $g'(\zeta)$ which can be physically attributed to the fact that augmentation in the porosity parameter elevates the resistance of the porous medium. Fig. 6.9 displays the positive impact of δ on $g'(\zeta)$. Physically, increment in the stretching rate enhances the momentum associated with the boundary layer that swells the y-directional velocity.

Fig. 6.10 reflects the rise in $\theta(\zeta)$ due to mounting ϕ_{Cu} values. This is because an increase in ϕ_{Cu} improves the thermal conductivity of the hybrid nanoliquid which triggers an improvement in $\theta(\zeta)$. Fig. 6.11 describes the deviations in $\theta(\zeta)$ concerning M. The applied magnetic field generates a Lorentz force that ascends the temperature profile. The increase in $\theta(\zeta)$ with respect to augmentation in Bi values is described in Fig. 6.12. Physically, augmentation in the Biot number implies increased convection which enhances the hybrid nanoliquid temperature.

Fig. 6.13 elucidates the consequence of M on $\phi(\zeta)$. An increase in M tends to

increase $\phi(\zeta)$. The enhancement in $\phi(\zeta)$ due to an increase in K_1 has been graphed in Fig. 6.14. Furthermore, a dual nature is observed for augmenting λ values. For larger values of ζ, a decrease in $\phi(\zeta)$ is noted.

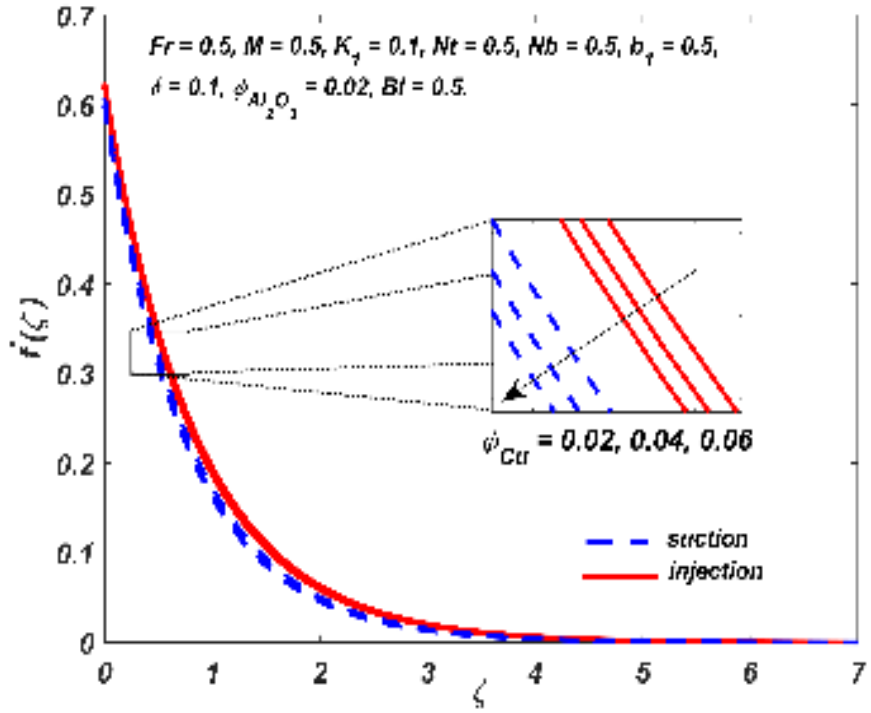

Figure 6.2: *Change in* $f'(\zeta)$ *for differing* ϕ_{Cu} *values.*

The simultaneous effect of two parameters on $Nu_x(Re_x)^{-\frac{1}{2}}$ is analysed with the aid of three-dimensional surface plots which have been graphed in Figs. 6.15 to 6.18. A comparative study between the suction and injection cases is also carried out. It can be perceived that the heat transfer rate is higher for the suction case in comparison with the injection case. From Figs. 6.15 to 6.18, it is seen that ϕ_{Cu} and Bi ascends $Nu_x(Re_x)^{-\frac{1}{2}}$ whereas Nt and M demotes the heat transfer rate. The key observations drawn from Tables 6.5 and 6.6 are:

- The drag coefficients $\left(Re_x^{\frac{1}{2}}\ Cf_x \text{ and } Re_y^{\frac{1}{2}}\ Cf_y\right)$ are directly proportional to b_1 and inversely proportional to M, K_1, and ϕ_{Cu}.
- $Re_x^{\frac{1}{2}}\ Cf_x$ is a decreasing function of Fr whereas $Re_y^{\frac{1}{2}}\ Cf_y$ is an increasing

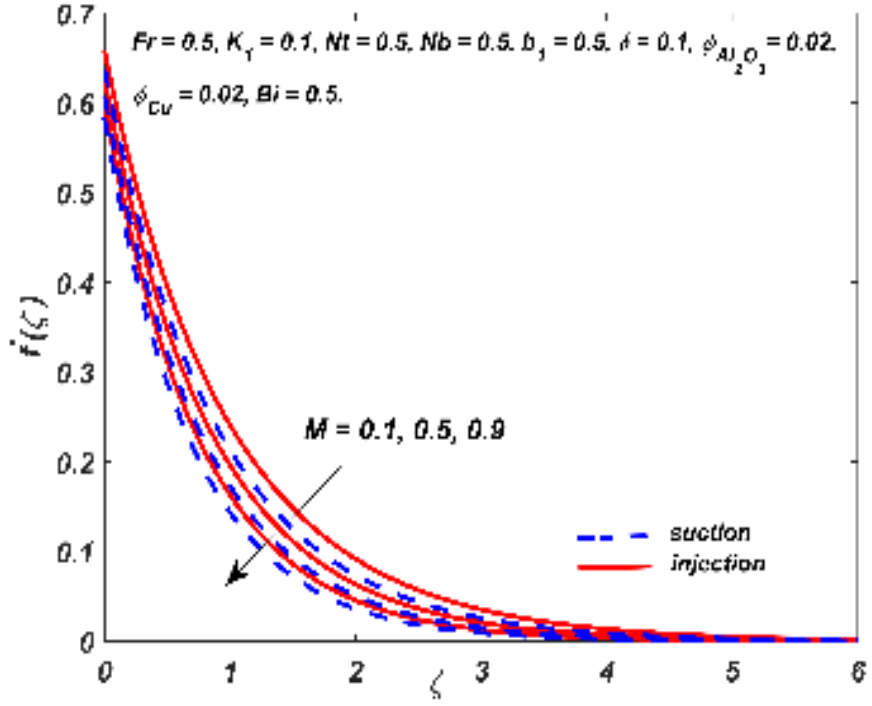

Figure 6.3: *Change in* $f'(\zeta)$ *for differing* M *values.*

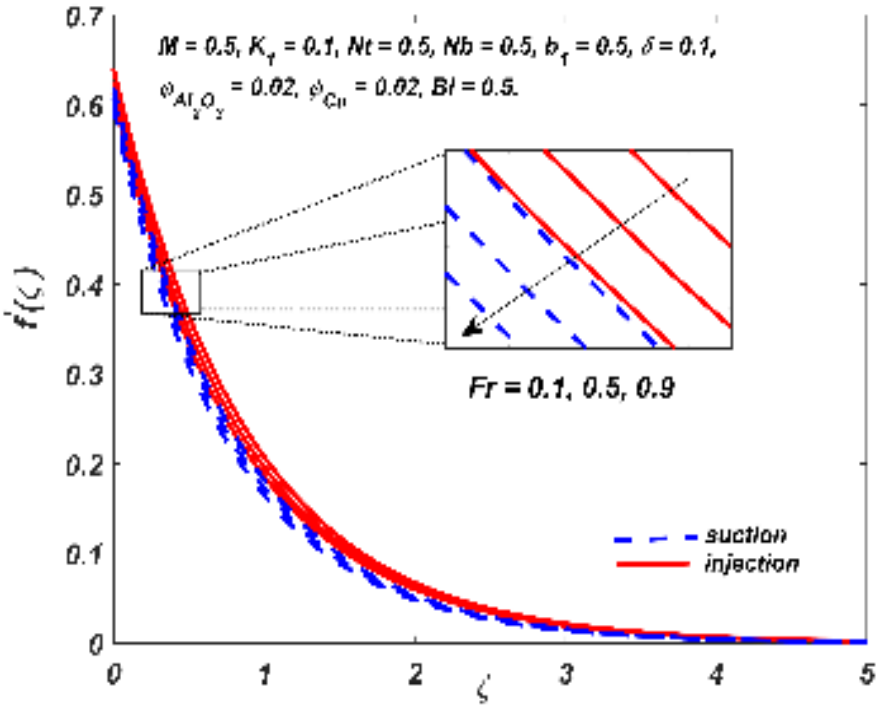

Figure 6.4: *Change in* $f'(\zeta)$ *for differing* Fr *values.*

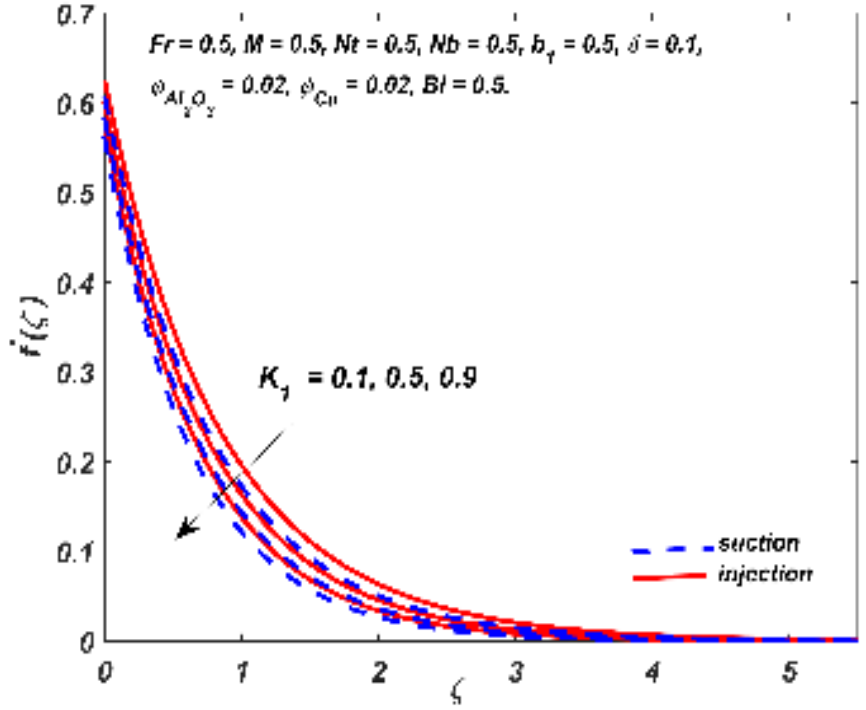

Figure 6.5: *Change in* $f'(\zeta)$ *for differing* K_1 *values.*

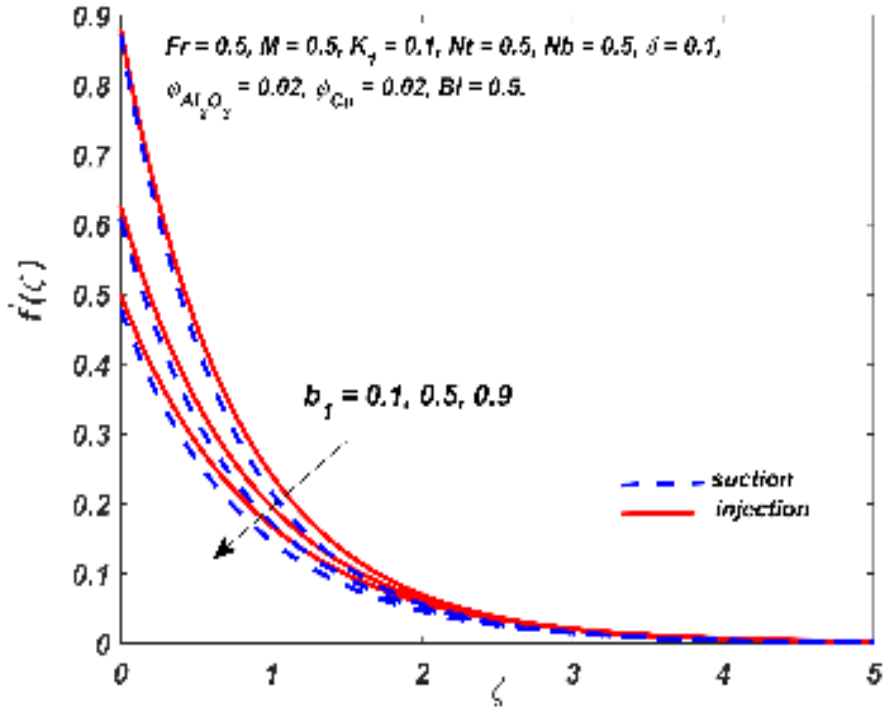

Figure 6.6: *Change in* $f'(\zeta)$ *for differing* b_1 *values.*

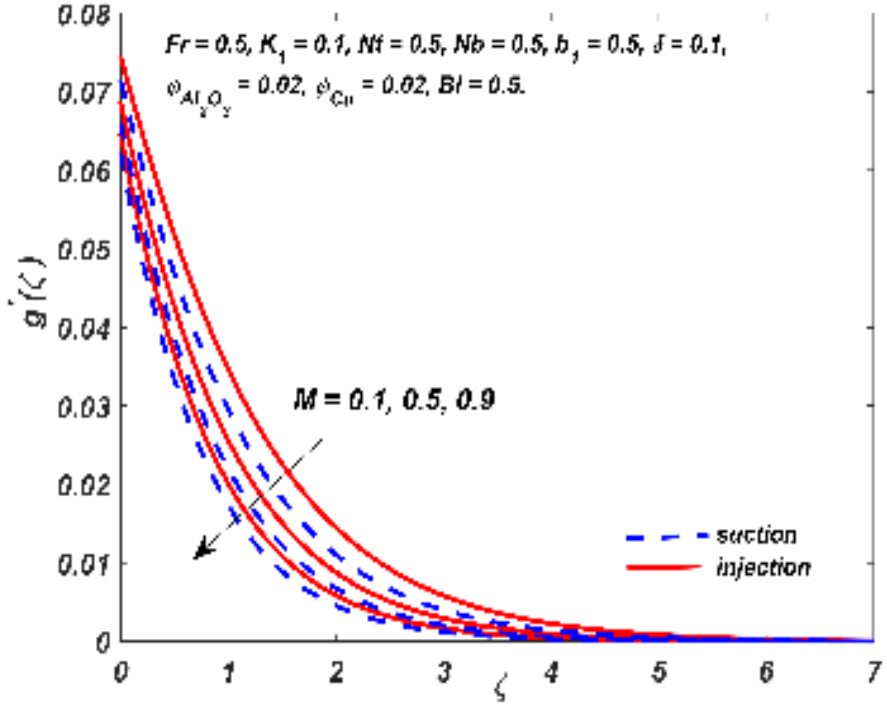

Figure 6.7: *Change in $g'(\zeta)$ for differing M values.*

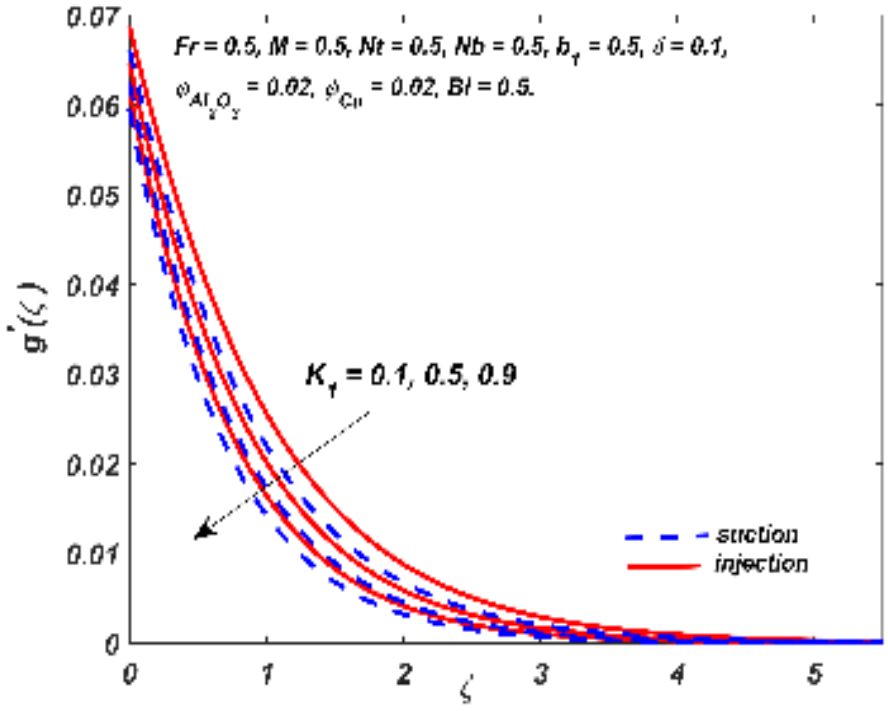

Figure 6.8: *Change in $g'(\zeta)$ for differing K_1 values.*

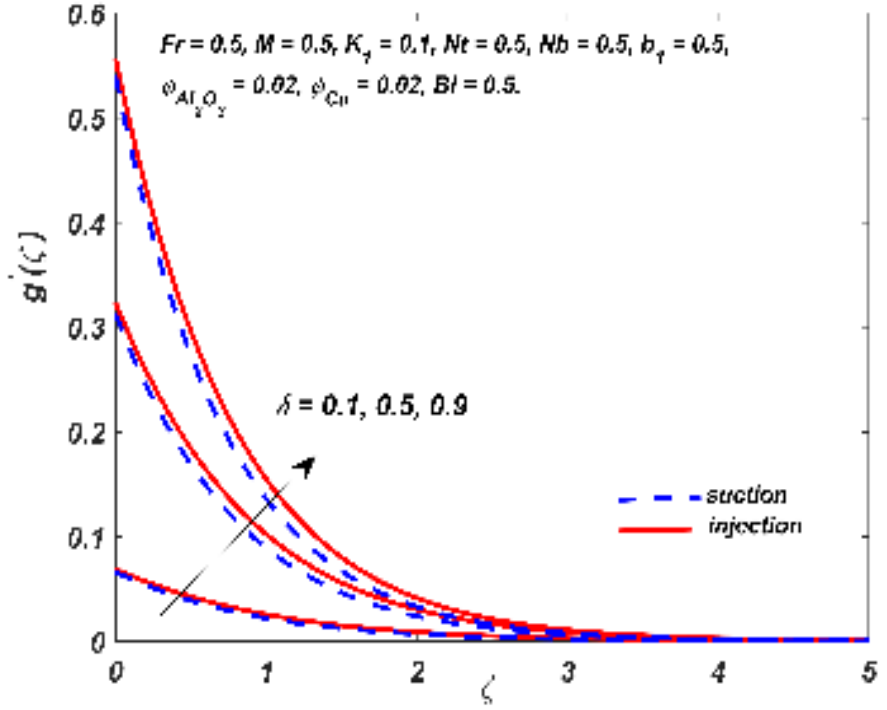

Figure 6.9: *Change in* $g'(\zeta)$ *for differing* δ *values.*

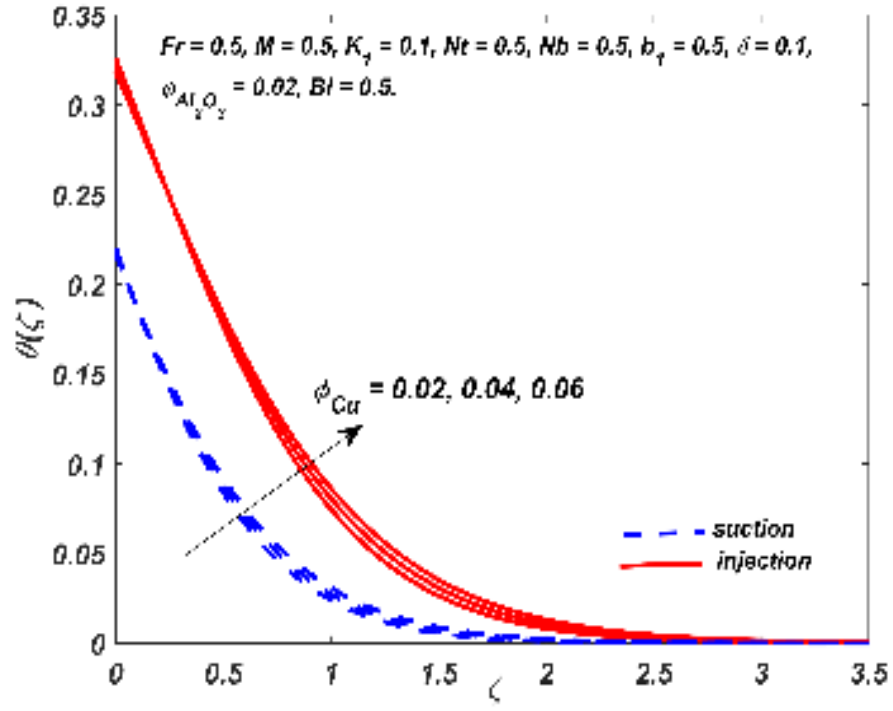

Figure 6.10: *Change in* $\theta(\zeta)$ *for differing* ϕ_{Cu} *values.*

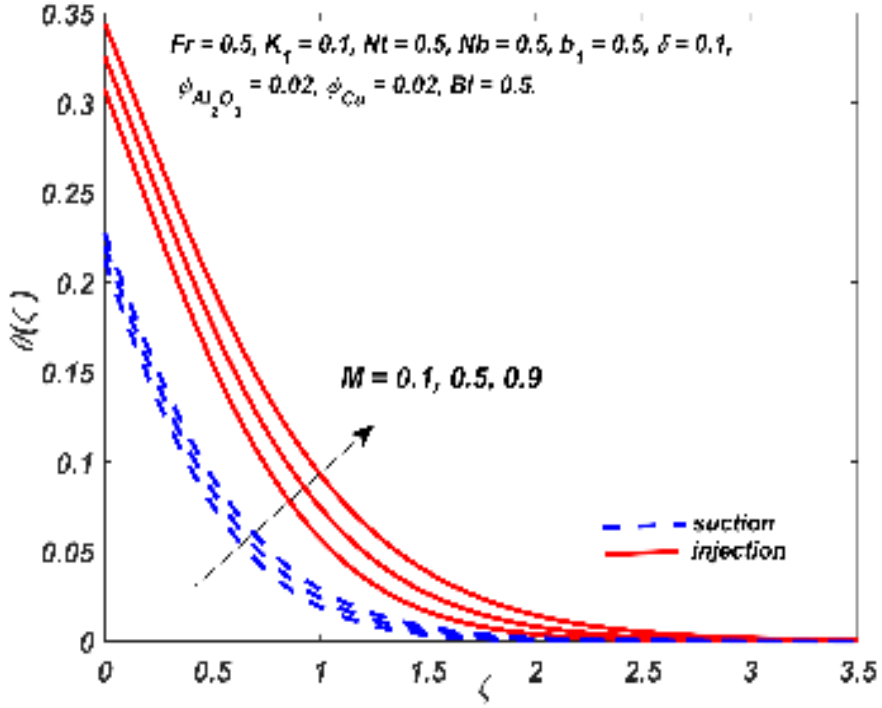

Figure 6.11: *Change in $\theta(\zeta)$ for differing M values.*

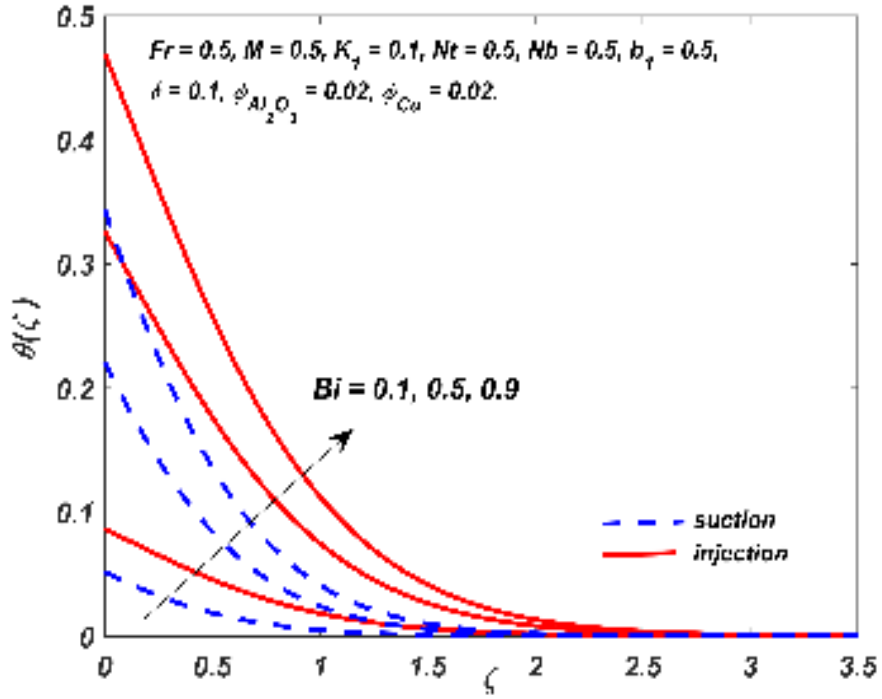

Figure 6.12: *Change in $\theta(\zeta)$ for differing Bi values.*

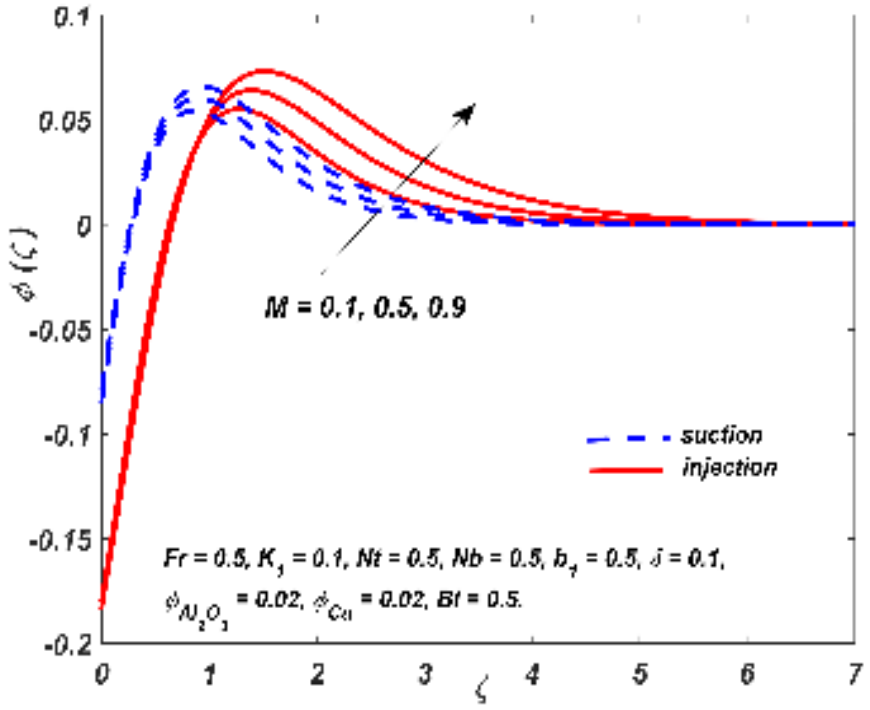

Figure 6.13: *Change in $\phi(\zeta)$ for differing M values.*

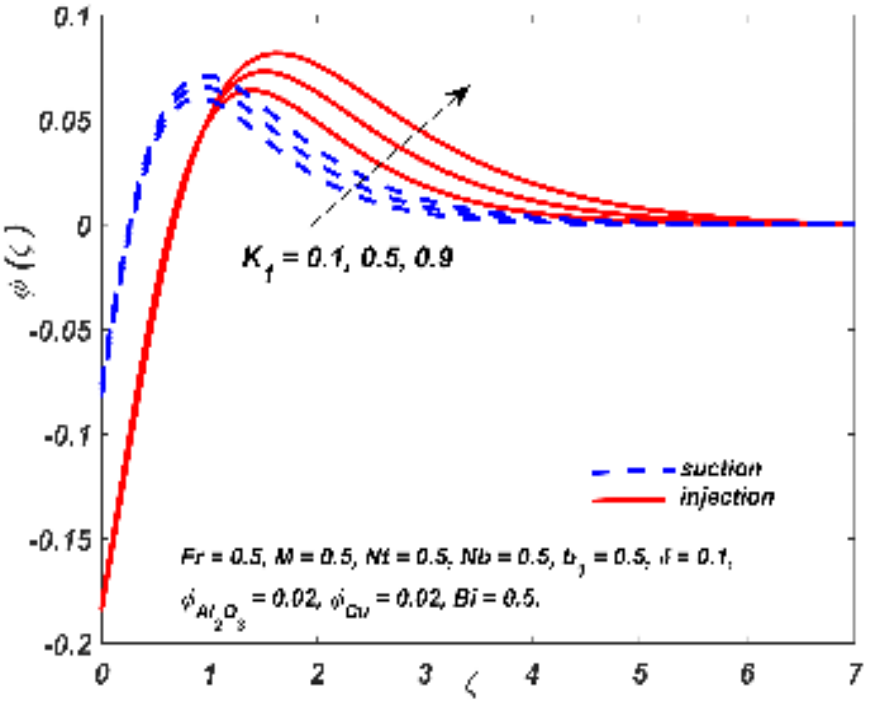

Figure 6.14: *Change in $\phi(\zeta)$ for differing K_1 values.*

Table 6.5: *Comparison on* $Re_x^{\frac{1}{2}}\ Cf_x$ *for differing values of* $Fr,\ M,\ K_1,\ \phi_{Cu}$, *and* b_1 *when* $Nt = 0.5,\ Nb = 0.5, \delta = 0.1, Bi = 0.5, \phi_{Al_2O_3} = 0.02$

					$Re_x^{\frac{1}{2}}\ Cf_x$	
Fr	M	K_1	ϕ_{Cu}	b_1	$\lambda = -0.1$	$\lambda = 0.1$
0.5	0.5	0.1	0.02	0.5	-0.82645	-0.86720
0.6	0.5	0.1	0.02	0.5	-0.83347	-0.87355
0.7	0.5	0.1	0.02	0.5	-0.84029	-0.87972
0.8	0.5	0.1	0.02	0.5	-0.84691	-0.88573
0.9	0.5	0.1	0.02	0.5	-0.85335	-0.89159
0.5	0.1	0.1	0.02	0.5	-0.75660	-0.80000
0.5	0.3	0.1	0.02	0.5	-0.79327	-0.83533
0.5	0.5	0.1	0.02	0.5	-0.82645	-0.86720
0.5	0.7	0.1	0.02	0.5	-0.85668	-0.89618
0.5	0.9	0.1	0.02	0.5	-0.88442	-0.92272
0.5	0.5	0.1	0.02	0.5	-0.82645	-0.86720
0.5	0.5	0.3	0.02	0.5	-0.85620	-0.89572
0.5	0.5	0.5	0.02	0.5	-0.88353	-0.92188
0.5	0.5	0.7	0.02	0.5	-0.90878	-0.94602
0.5	0.5	0.9	0.02	0.5	-0.93223	-0.96842
0.5	0.5	0.1	0.02	0.5	-0.82645	-0.86720
0.5	0.5	0.1	0.035	0.5	-0.86654	-0.91058
0.5	0.5	0.1	0.05	0.5	-0.90787	-0.95520
0.5	0.5	0.1	0.065	0.5	-0.95063	-1.00126
0.5	0.5	0.1	0.08	0.5	-0.99499	-1.04893
0.5	0.5	0.1	0.02	0.5	-0.82645	-0.86720
0.5	0.5	0.1	0.02	0.6	-0.76009	-0.79558
0.5	0.5	0.1	0.02	0.7	-0.70426	-0.73557
0.5	0.5	0.1	0.02	0.8	-0.65655	-0.68446
0.5	0.5	0.1	0.02	0.9	-0.61526	-0.64036

function of δ.

- Similar results are obtained for suction and injection cases.

- Higher drag coefficients are observed in the injection case when compared with the suction case.

6.5 Special Cases

In this section, a restrictive analysis on the velocity profile has been elucidated. The heat and concentration equations have been ignored for this purpose. A comparative analysis on the two-dimensional and axisymmetric flows considering slip and no-slip

Table 6.6: *Comparison on* $Re_y^{\frac{1}{2}}\ Cf_y$ *for differing values of* $M,\ K_1,\ \phi_{Cu},\ b_1$ *and* δ *when* $Nt = 0.5,\ Nb = 0.5, Fr = 0.5, Bi = 0.5, \phi_{Al_2O_3} = 0.02$.

					$Re_y^{\frac{1}{2}}\ Cf_y$	
M	K_1	ϕ_{Cu}	b_1	δ	λ = -0.1	$\lambda = 0.1$.
0.1	0.1	0.02	0.5	0.1	-1.77802	-1.99400
0.3	0.1	0.02	0.5	0.1	-2.00464	-2.19939
0.5	0.1	0.02	0.5	0.1	-2.18844	-2.36760
0.7	0.1	0.02	0.5	0.1	-2.34321	-2.51015
0.9	0.1	0.02	0.5	0.1	-2.47692	-2.63389
0.5	0.1	0.02	0.5	0.1	-2.18844	-2.36760
0.5	0.3	0.02	0.5	0.1	-2.34083	-2.50795
0.5	0.5	0.02	0.5	0.1	-2.47276	-2.63003
0.5	0.7	0.02	0.5	0.1	-2.58907	-2.73804
0.5	0.9	0.02	0.5	0.1	-2.69305	-2.83487
0.5	0.1	0.02	0.5	0.1	-2.18844	-2.36760
0.5	0.1	0.035	0.5	0.1	-2.28573	-2.48110
0.5	0.1	0.05	0.5	0.1	-2.38688	-2.59846
0.5	0.1	0.065	0.5	0.1	-2.49229	-2.72008
0.5	0.1	0.08	0.5	0.1	-2.60233	-2.84636
0.5	0.1	0.02	0.5	0.1	-2.18844	-2.36760
0.5	0.1	0.02	0.6	0.1	-2.04495	-2.20318
0.5	0.1	0.02	0.7	0.1	-1.92046	-2.06148
0.5	0.1	0.02	0.8	0.1	-1.81124	-1.93790
0.5	0.1	0.02	0.9	0.1	-1.71453	-1.82904
0.5	0.1	0.02	0.5	0.1	-2.18844	-2.36760
0.5	0.1	0.02	0.5	0.3	-1.35288	-1.44597
0.5	0.1	0.02	0.5	0.5	-1.10429	-1.17061
0.5	0.1	0.02	0.5	0.7	-0.97353	-1.02581
0.5	0.1	0.02	0.5	0.9	-0.88932	-0.93275

constraints is presented through Figs. 6.19 and 6.20.

6.5.1 Two-dimensional flow

The momentum equation of a two-dimensional flow ($g = 0$ and $\delta = 0$) is given by:

$$\left.\begin{array}{c} f''' - \left(\frac{A_2}{A_1}\right)\left\{(1+Fr)\,f'^2 - ff''\right\} - \left(\frac{A_3}{A_1}M + \lambda\right)f' = 0. \\ f'(0) = 1, f(0) = \lambda, f'(\infty) \to 0 \ \ (no\ slip\ condition) \\ f'(0) = 1 + b_1 f''(0)\,, f(0) = \lambda, f'(\infty) \to 0 \ \ (\ slip\ condition) \end{array}\right\} \tag{6.5.1}$$

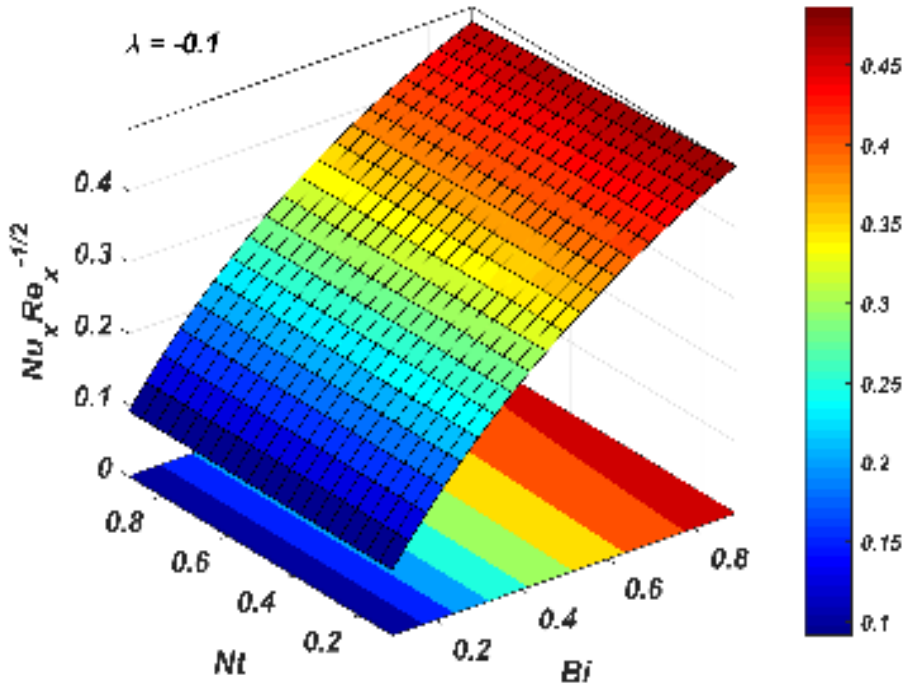

Figure 6.15: *Change in* $Nu_x(Re_x)^{-\frac{1}{2}}$ *for differing* Nt *and* Bi *with* $\lambda = -0.1$.

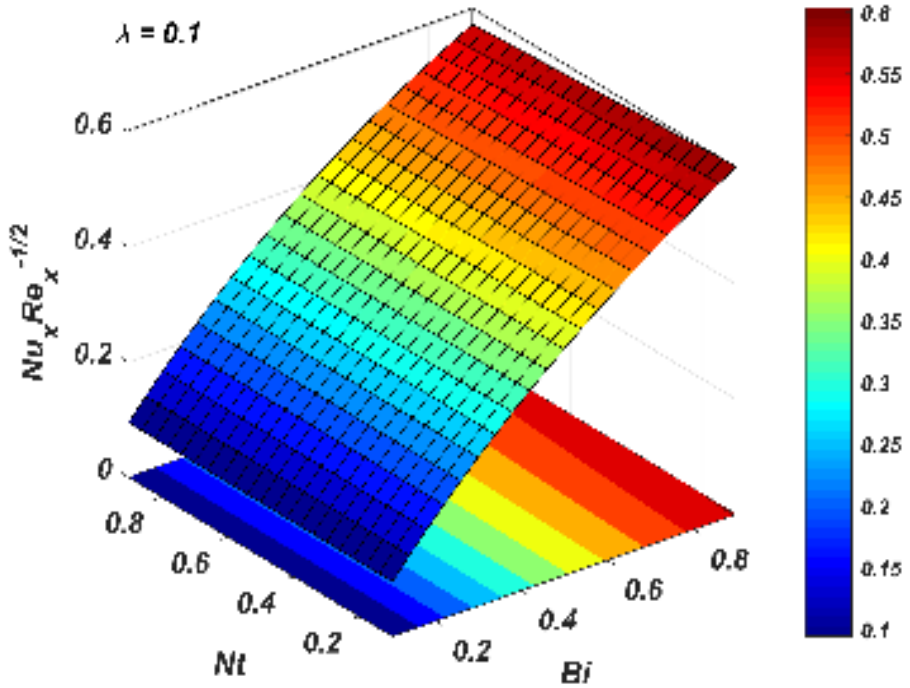

Figure 6.16: *Change in* $Nu_x(Re_x)^{-\frac{1}{2}}$ *for differing* Nt *and* Bi *with* $\lambda = 0.1$.

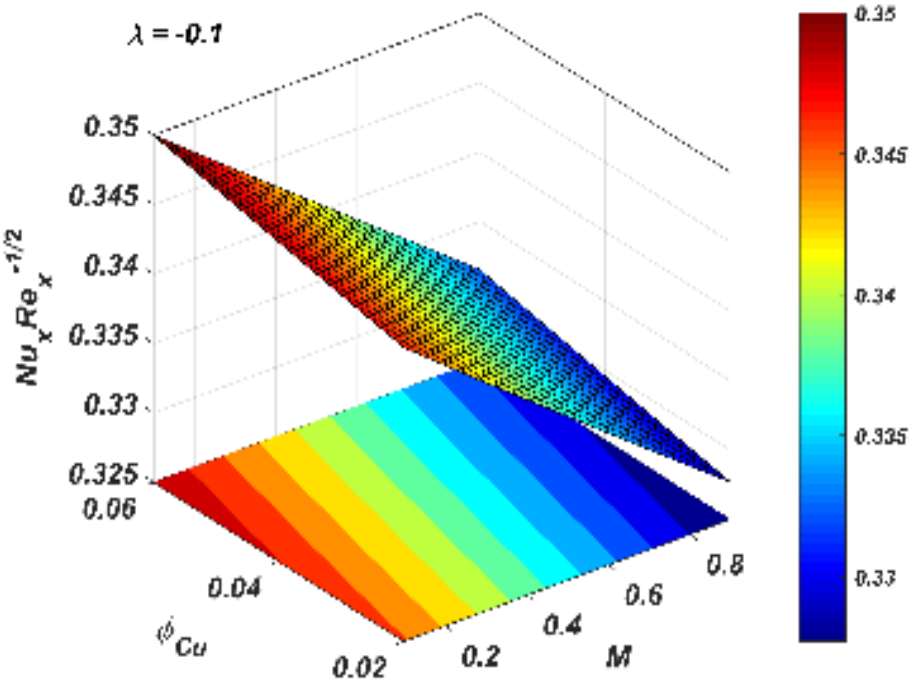

Figure 6.17: *Change in* $Nu_x(Re_x)^{-\frac{1}{2}}$ *for differing* ϕ_{Cu} *and* M *with* $\lambda = -0.1$.

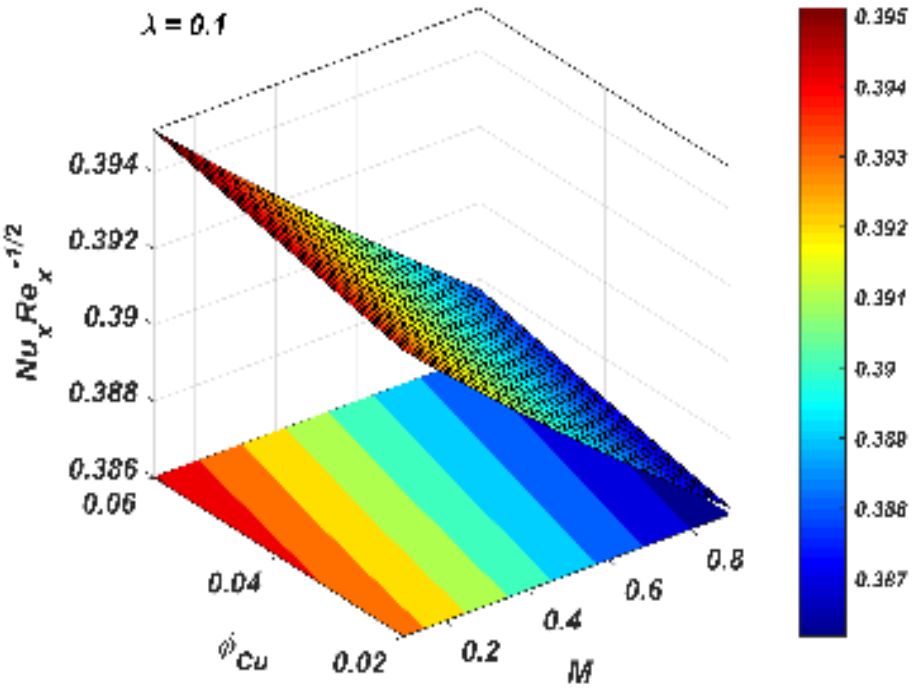

Figure 6.18: *Change in* $Nu_x(Re_x)^{-\frac{1}{2}}$ *for differing* ϕ_{Cu} *and* M *with* $\lambda = 0.1$.

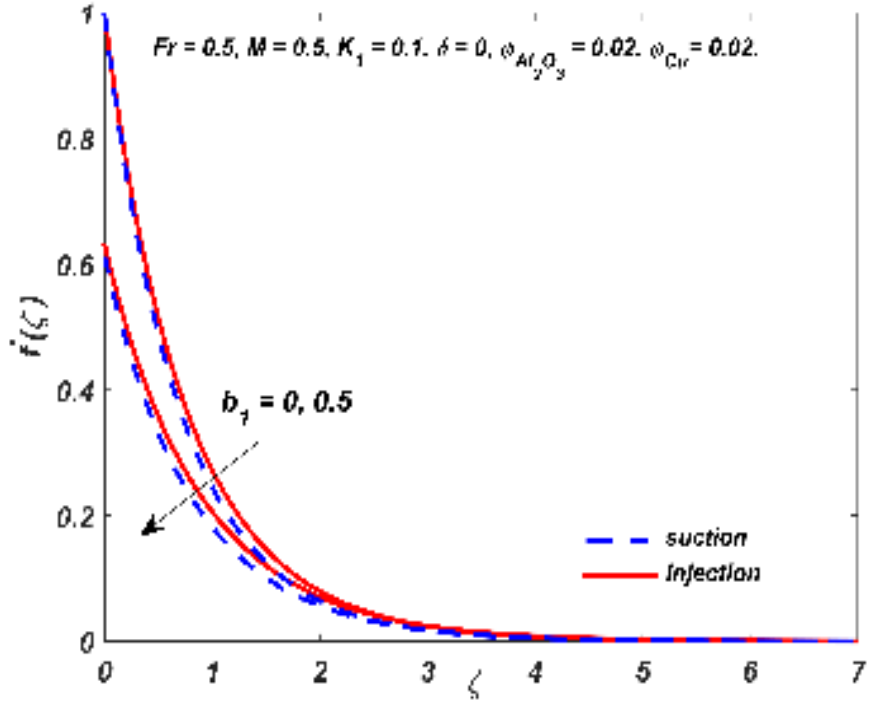

Figure 6.19: *Change in $f'(\zeta)$ of the two-dimensional flow for differing b_1 values.*

6.5.2 Axisymmetric flow

The momentum equation of an axisymmetric flow ($f = g$ and $\delta = 1$) is given by:

$$\left.\begin{array}{c} f''' - \left(\frac{A_2}{A_1}\right)\left\{(1+Fr)\,f'^2 - 2ff''\right\} - \left(\frac{A_3}{A_1}M + \lambda\right)f' = 0. \\ f'(0) = 1, f(0) = \lambda, f'(\infty) \to 0 \ \ (no\ slip\ condition) \\ f'(0) = 1 + b_1 f''(0), f(0) = \lambda, f'(\infty) \to 0 \ \ (\ slip\ condition) \end{array}\right\} \tag{6.5.2}$$

Fig. 6.19 depicts the effect of b_1 and λ on the two-dimensional flow. A higher velocity profile is observed in the case of injection and no-slip conditions. The impact of b_1 and λ on the axisymmetric flow have been illustrated using Fig. 6.20. A lower velocity profile is observed in the case of suction and slip conditions.

6.6 Regression Analysis

Regression analysis helps in establishing the relationship between a dependent and one or more independent variables . In this study, the relationship between the drag coefficients and the pertinent parameters for suction ($\lambda = 0.1$) and injection

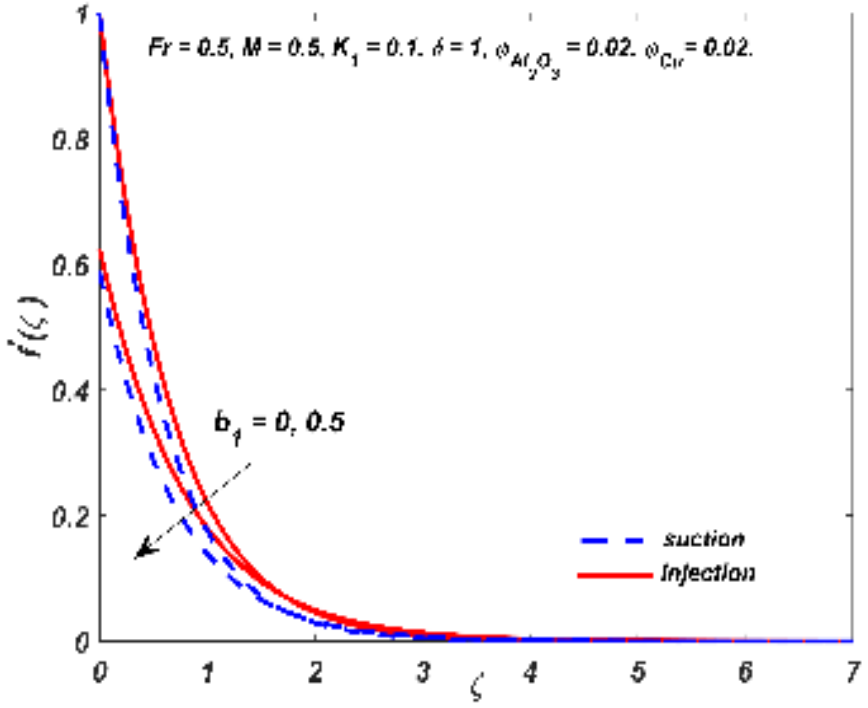

Figure 6.20: *Change in $f'(\zeta)$ of the axisymmetric flow for differing b_1 values.*

($\lambda = -0.1$) cases has been statistically modelled. The general form for the estimated model is given by:

$$Re_x^{\frac{1}{2}}\ Cf_x\ = r_{Fr}Fr + r_M M + r_{K_1}K_1 + r_{\phi_{Cu}}\phi_{Cu} + r_{b_1}b_1 + c \tag{6.6.1}$$

$$Re_y^{\frac{1}{2}}\ Cf_y\ = r_M M + r_{K_1}K_1 + r_{\phi_{Cu}}\phi_{Cu} + r_{b_1}b_1 + r_\delta\delta + c \tag{6.6.2}$$

where r_{Fr}, r_M, r_{K_1}, $r_{\phi_{Cu}}$, r_{b_1}, r_δ and c are the estimated regression coefficients. The drag coefficients are estimated using the 25 sets of values chosen in the range $[0.1, 0.9]$ for δ, $[0.5, 0.9]$ for b_1 , $[0.1, 0.9]$ for K_1, $[0.02, 0.08]$ for ϕ_{Cu} , $[0.5, 0.9]$ for Fr, and $[0.1, 0.9]$ for M and the regression coefficients are found using the MATLAB software. The estimated regression models are given by:

$$\begin{aligned} Re_x^{\frac{1}{2}}\ {Cf_x}^{\lambda=-0.1}\ &= -0.07585\ Fr - 0.15952\ M - 0.13964\ K_1 - 2.82993\ \phi_{Cu} \\ &\quad +0.547116\ b_1 - \ 0.90938 \end{aligned} \tag{6.6.3}$$

$$Re_y^{\frac{1}{2}}\ Cf_y{}^{\lambda=-0.1} = -0.86819\ M - 0.74863\ K_1 - 8.02595\ \phi_{Cu} + 1.052088\ b_1 + 1.882442\ \delta - 2.17821 \tag{6.6.4}$$

$$Re_x^{\frac{1}{2}}\ Cf_x{}^{\lambda=0.1} = -0.06984\ Fr - 0.15314\ M - 0.13403\ K_1 - 3.05209\ \phi_{Cu} + 0.588495\ b_1 - 0.97302 \tag{6.6.5}$$

$$Re_y^{\frac{1}{2}}\ Cf_y{}^{\lambda=0.1} = -0.79527\ M - 0.70502\ K_1 - 9.18266\ \phi_{Cu} + 1.211844\ b_1 + 2.082646\ \delta - 2.47155 \tag{6.6.6}$$

The sign of the estimated regression coefficient denotes the nature of the relationship for the corresponding parameter on the dependent variable and the magnitude of the estimated regression coefficient corresponds to the intensity of this relationship. From the estimated models it is conclusive that the relationship experienced by the influential parameters on the drag coefficients are in present harmony with the observations derived from Tables 6.5 and 6.6. Figs. 6.21 to 6.24 illustrate the accuracy of the regression model for the chosen sample. A commendable agreement is noted between the actual and estimated values.

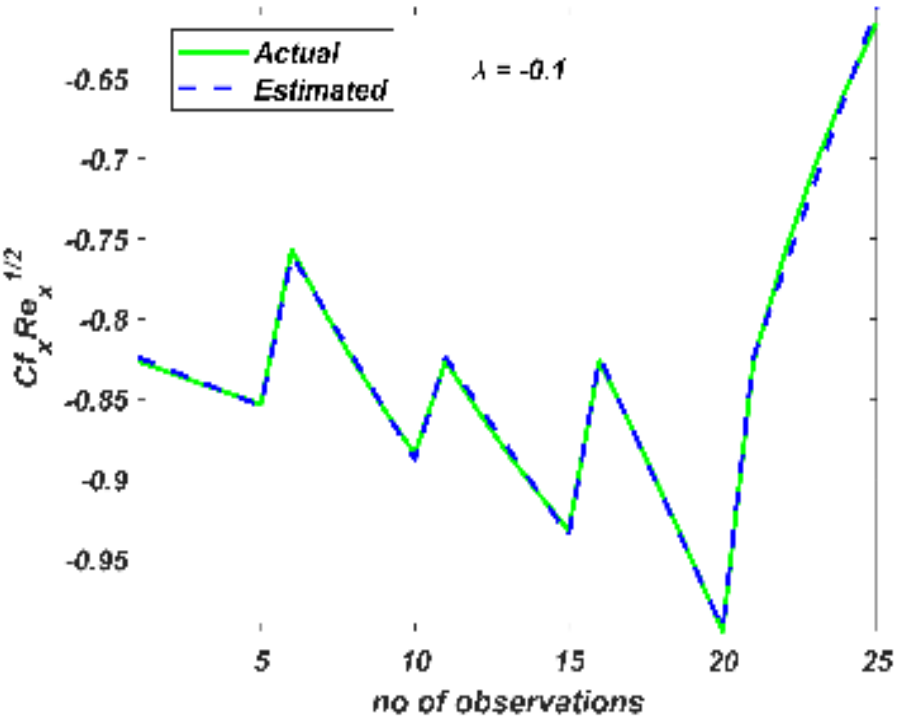

Figure 6.21: *Actual* $Re_x^{\frac{1}{2}} Cf_x$ *versus Estimated* $Re_x^{\frac{1}{2}} Cf_x$ *with* $\lambda = -0.1$.

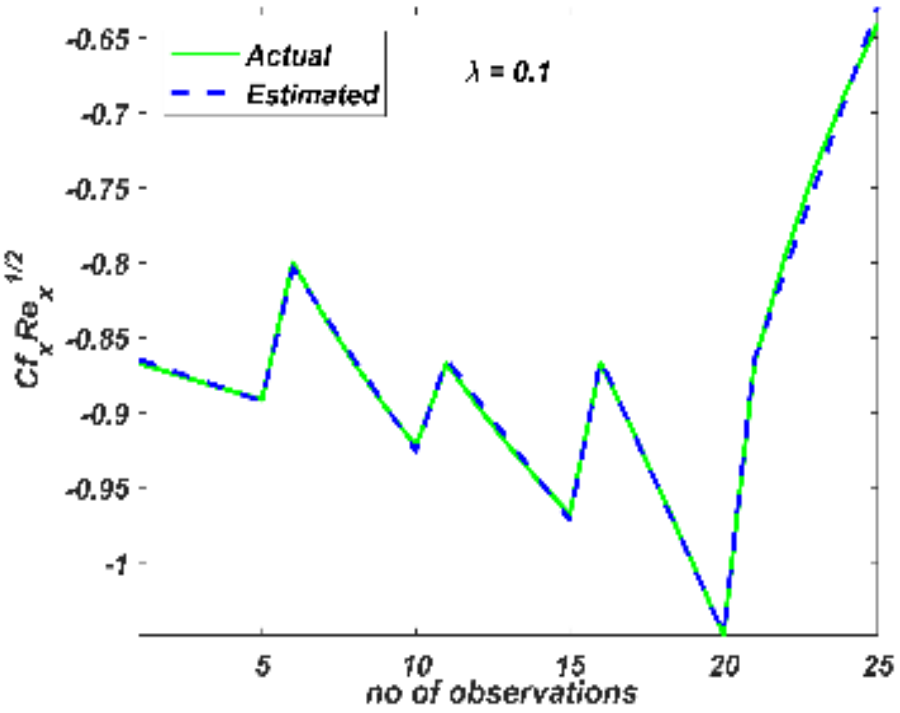

Figure 6.22: *Actual* $Re_x^{\frac{1}{2}} Cf_x$ *versus Estimated* $Re_x^{\frac{1}{2}} Cf_x$ *with* $\lambda = 0.1$.

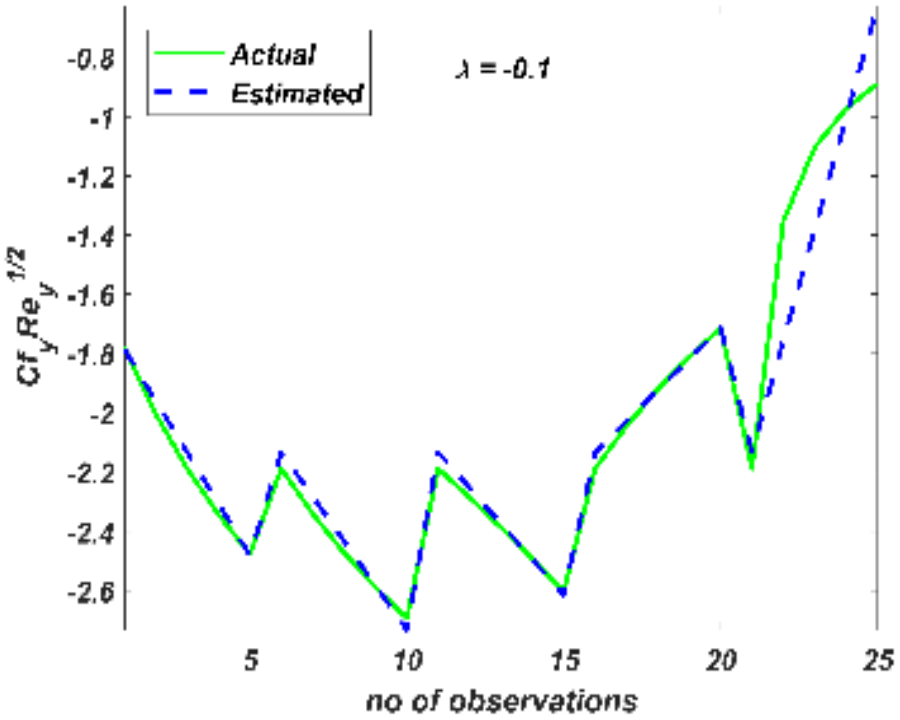

Figure 6.23: *Actual* $Re_y^{\frac{1}{2}} Cf_y$ *versus Estimated* $Re_y^{\frac{1}{2}} Cf_y$ *with* $\lambda = -0.1$.

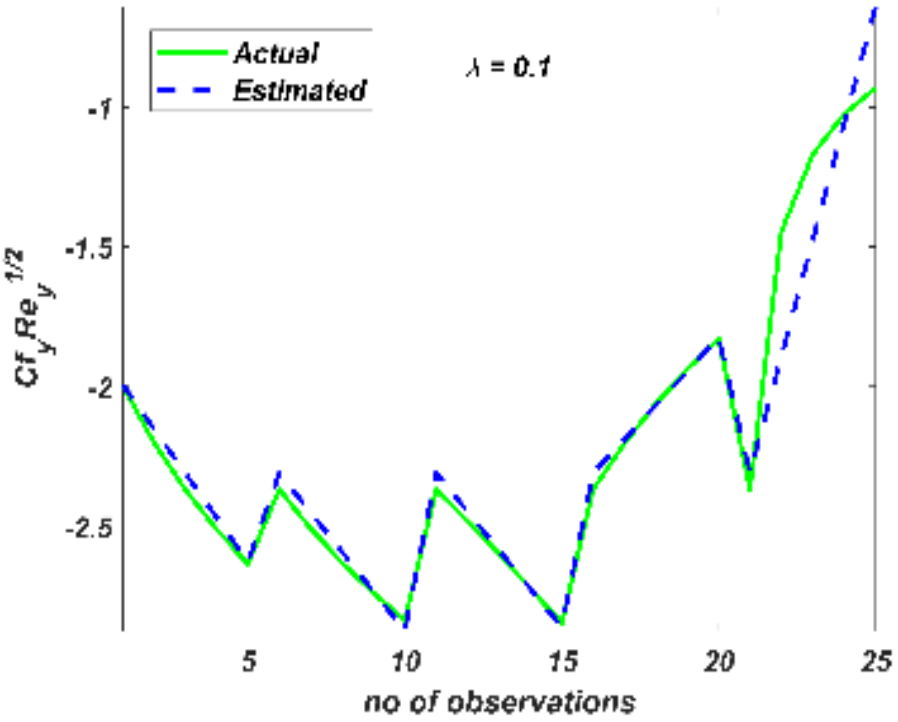

Figure 6.24: *Actual* $Re_y^{\frac{1}{2}} Cf_y$ *versus Estimated* $Re_y^{\frac{1}{2}} Cf_y$ *with* $\lambda = 0.1$.

6.7 Conclusions

For its applications in astronomical disciplines, fuel injection, solar collector plate, thermal protection, and aerodynamics; the MHD Darcy-Forchheimer hybrid nanoliquid flow over an elongated permeable sheet in a porous medium with hydrodynamic slip and Newtonian boundary constraints have been examined. A realistic model is used by considering the passive control of nanoparticles and the modified Buongiorno nanoliquid model. The consequence of effectual parameters on the flow profiles has been numerically investigated using the bvp5c routine. A comparative analysis of the velocity profile on the two-dimensional and axisymmetric flows in the presence of slip and no-slip constraints has also been presented. Further, the relationship between the pertinent parameters and the drag coefficients has been statistically scrutinized utilizing regression analysis. The major conclusions drawn from the study are:

- The x-directional velocity descends with the Forchheimer number and hydrodynamic slip parameter.

- The y-directional velocity ascends with the stretching parameter.
- The suction case exhibits lowered temperature and velocity profiles in correspondence with the injection case.
- The Biot number and the volume fraction of copper nanoparticles have a constructive effect on the hybrid nanoliquid temperature.
- The heat transfer rate is higher for the suction case in comparison with the injection case.
- The heat transfer rate is higher for lower values of magnetic field parameter and higher values of Biot number and volume fraction of copper nanoparticles.
- The drag coefficients increase with hydrodynamic slip parameter and decrease for higher values of magnetic field and porosity parameters.
- Higher drag coefficients are observed in the case of injection when compared with the suction case.
- A commendable agreement is noted between the numerical and statistical results.